

Evolution of Accretion Disk Structure of the Black Hole X-ray Binary MAXI J1820+070 during the Rebrightening Phase

Tomohiro YOSHITAKE¹, Megumi SHIDATSU², Yoshihiro UEDA¹, Daisaku NOGAMI¹, Katsuhiro L. MURATA³, Narikazu HIGUCHI⁴, Keisuke ISOGAI^{3, 5}, Hiroyuki MAEHARA^{3,4}, Shin MINESHIGE¹, Hitoshi NEGORO⁶, Nobuyuki KAWAI⁴, Yoichi YATSU⁴, Mahito SASADA⁴, Ichiro TAKAHASHI⁴, Masafumi NIWANO⁴, Tomoki SAITO⁷, Masaki TAKAYAMA⁷, Yumiko OASA^{8,9}, Takuya TAKARADA^{9,10}, Takumi SHIGEYOSHI⁸ and OISTER Collaboration

¹Department of Astronomy, Kyoto University, Kitashirakawa-Oiwake-cho, Sakyo-ku, Kyoto, Kyoto 606-8502, Japan

²Department of Physics, Ehime University, 2-5, Bunkyocho, Matsuyama, Ehime 790-8577, Japan

³Okayama Observatory, Kyoto University, 3037-5 Honjo, Kamogatacho, Asakuchi, Okayama 719-0232, Japan

⁴Department of Physics, Tokyo Institute of Technology, 2-12-1 Ookayama, Meguro-ku, Tokyo 152-8551, Japan

⁵Department of Multi-Disciplinary Sciences, Graduate School of Arts and Sciences, The University of Tokyo, 3-8-1 Komaba, Meguro, Tokyo 153-8902, Japan

⁶Department of Physics, Nihon University, 1-8-14 Kanda-Surugadai, Chiyoda-ku, Tokyo 101-8308, Japan

⁷Nishi-Harima Astronomical Observatory, Center for Astronomy, University of Hyogo, 407-2 Nishigaichi, Sayo-cho, Sayo, Hyogo 679-5313, Japan

⁸Faculty of education, Saitama University, Simo-okubo 255, Sakura-ku, Saitama 338-8570, Japan

⁹Graduate School of Science and Engineering, Saitama University, Simo-okubo 255, Sakura-ku, Saitama 338-8570, Japan

¹⁰Astrobiology Center, NINS, 2-21-1 Osawa, Mitaka, Tokyo 181-8588, Japan

*E-mail: yoshitake@kusastro.kyoto-u.ac.jp

Received (reception date); Accepted (acceptation date)

Abstract

To understand the evolution of global accretion disk structure in the “rebrightening” phase of MAXI J1820+070, we perform a comprehensive analysis of its near infrared/optical/UV to X-ray spectral energy distribution (SED) utilizing data obtained by OISTER, Las Cumbres Observatory (LCO), Swift, NICER, and NuSTAR in 2019. Optical spectra observed with Seimei telescope in 2019 and 2020 are also analyzed. On the basis of the optical and X-ray light curves and their flux ratios, we divide the whole phase into 3 periods, Periods I (flux rise), II (decay), and III (dim). In the first 2 periods, the source stayed in the low/hard state (LHS), where the X-ray (0.3–30 keV) and optical/UV SED can be both fitted with power-law models. We interpret that the X-ray emission arises from hot corona via Comptonization, whereas the

optical/UV flux is dominated by synchrotron radiation from the jets, with a partial contribution from the irradiated disk. The optical/UV power-law component smoothly connects to a simultaneous radio flux, supporting its jet origin. Balmer line profiles in the optical spectra indicate that the inner radius of an irradiated disk slightly decreased from $\sim 2 \times 10^5 r_g$ (Period I) to $\sim 1 \times 10^5 r_g$ (Period II), where r_g is the gravitational radius, implying a change of the hot corona geometry. In Period III, the SED can be reproduced by an advection-dominated accretion flow and jet emission. However, the double-peaked $H\alpha$ emission line indicates that a cool disk remained at large radii.

Key words: X-rays: individual (MAXI J1820+070) — X-rays: binaries — accretion, accretion disks — black hole physics

1 Introduction

Many Galactic black hole X-ray binaries (BHXB) have a transient nature. They suddenly exhibit outbursts and increase their X-ray luminosity by several orders of magnitude (e.g., Tanaka & Shibazaki 1996; Tetarenko et al. 2016). These large outbursts are often followed by one or more rebrightenings (or “mini-outbursts”) whose peak fluxes are usually lower than the main outbursts (Muñoz-Darias et al. 2017; Cúneo et al. 2020; Zhang et al. 2019; Saikia et al. 2023). The X-rays from BHXBs are produced by the release of the gravitational energy of the accreted gas, and the luminosity is considered to reflect the mass accretion rate. Therefore, monitoring BHXBs during their outburst/rebrightening periods gives us insight on how the black hole accretion disk evolves with the mass accretion rate.

Intensive observations, mainly in the X-ray band, have been revealing the accretion disk structure at high luminosities. After the outburst rise, BHXBs show the state transition from the low/hard state (LHS) to the high/soft state (HSS), where a hard, power-law shaped X-ray spectrum changes to a thermal spectrum dominating the soft X-ray band. This transition is generally explained by the change in the inner disk structure (see e.g., Done et al. 2007). In the LHS, the standard disk (Shakura & Sunyaev 1973), which is an optically thick and geometrically thin accretion disk, is replaced by a hot, radiatively inefficient inner flow (RIAF) in the vicinity of the black hole (e.g., Makishima et al. 2008), while in the HSS, the standard disk extends down to the innermost stable circular orbit (e.g., Ebisawa et al. 1993). However, studies at low luminosities, especially below an X-ray luminosity of $L_X \sim 10^{36}$ erg s^{-1} , is limited so far. Although in theory, the outburst evolution of the disk is generally explained by the disk instability model (Mineshige & Wheeler 1989; Lasota 2001), observational studies are limited to answer questions such as when the disk instability occurs at the outer disk region

and how the standard disk extends inwards, replacing the RIAF, with increasing mass accretion rate.

Multi-wavelength observations are key to understand the whole picture of the accretion disk structure and its evolution, because the disks in BHXBs emit photons not only in X-rays but also different wavelengths. They mainly emit X-ray photons in the vicinity of the black hole, while the outer regions of the disks predominantly produce ultraviolet (UV), optical, and near-infrared (IR) emission. Previous studies based on multi-wavelength spectral energy distribution (SED) suggest that the outer disk regions are heated by significant X-ray irradiation, resulting in enhancement of optical and near-IR fluxes (Gierliński et al. 2008; Gierliński et al. 2009). Strong X-ray irradiation can develop a hot, ionized atmosphere above the disk (e.g., Jimenez-Garate et al. 2002) and produce emission lines in the UV, optical, and near-IR bands. The lines usually show a double-peaked profile, due to the Keplerian motion of the gas in the line emitting region (Horne & Marsh 1986). It can also drive powerful disk winds (Begelman et al. 1983). Indeed, previous X-ray, optical, and near-IR spectroscopy of BHXBs detected blueshifted absorption lines (or P Cygni profiles), suggestive of the presence of disk winds (e.g., Ueda et al. 1998; Muñoz-Darias et al. 2016; Sánchez-Sierras & Muñoz-Darias 2020). These results demonstrate that multi-wavelength studies are essential for full understanding of black hole accretion and outflows.

MAXI J1820 is a Galactic BHXB discovered with Monitor of All-sky X-ray Image (MAXI; Matsuoka et al. 2009) in 2018 (Kawamuro et al. 2018; Shidatsu et al. 2018; Tucker et al. 2018). After the main outburst in 2018 with state transitions between the HSS and LHS (e.g., Shidatsu et al. 2019), it showed several rebrightening events, during which no state transitions to the HSS were reported. These outburst and rebrightening events were intensively observed at various wavelengths and using various methods, including multi-wavelength SED modeling (Rodi et al.

2021; Özbey Arabacı et al. 2022; Echiburú-Trujillo et al. 2023) and spectroscopy of optical emission and absorption lines (Muñoz-Darias et al. 2019; Sánchez-Sierras & Muñoz-Darias 2020; Sai et al. 2021; Koljonen et al. 2023; Tetarenko et al. 2023). In Yoshitake et al. (2022), we used a near-IR to X-ray SED and optical spectrum taken at an X-ray luminosity of $\sim 10^{33}$ erg s $^{-1}$ in the first rebrightening in 2019, and found that the emission from the advection-dominant accretion flow (ADAF) is dominant over the entire bands at this epoch.

In this article, we compile the multi-wavelength SEDs of MAXI J1820 obtained at different luminosities in the 2019 and 2020 rebrightenings, and investigate the evolution of the disk structure at low mass accretion rates, with an X-ray luminosity range of $\sim 6 \times 10^{32}$ erg s $^{-1} < L_X \lesssim 6 \times 10^{35}$ erg s $^{-1}$ (which corresponds to an Eddington ratio of $\sim 10^{-6} < L_X/L_{Edd} \lesssim 10^{-3}$). In addition, we use optical spectra obtained during these rebrightenings, to identify emission and absorption lines and study the line profiles and their variation with X-ray luminosity. In this work, we assume a distance of $D = 3$ kpc (Gandhi et al. 2019), a black hole mass of $M = 7-8 M_{\odot}$, and an inclination angle of $i = 69^{\circ}-77^{\circ}$ (Torres et al. 2019a) for MAXI J1820.

2 Observations and Data Reduction

We collected multi-wavelength data of MAXI J1820 obtained with various observatories in the first rebrightening period in 2019. We used X-ray data taken by the *Swift*/XRT, *NuSTAR* and *NICER*, UV data from the *Swift*/UVOT, and optical and near-IR photometric data from telescopes of Las Cumbres Observatory (LCO) and those in the Optical and Infrared Synergetic Telescopes for Education and Research (OISTER) collaboration. We also performed optical spectroscopic observations occasionally with *Seimei* telescope in the 2019 and 2020 rebrightenings. Table 1 and Table 2 give a log of the X-ray and UV observations and that of the optical and near-IR observations, respectively. Note that there are more LCO, *Swift*, and *NICER* observations than those listed in the tables, but we omitted the ones without sufficient simultaneous multi-wavelength coverage (see Section 3.2 for more detail).

2.1 *Swift*

The time-averaged *Swift*/XRT spectrum in the individual OBSID were obtained via the XRT on-demand web interface¹. The XRT data that we used were obtained either of the two CCD readout mode: the Photon Counting (PC) mode, which provides 2 dimensional spatial information, or

¹https://www.swift.ac.uk/user_objects/

the Windowed Timing (WT) mode, which retains only 1-dimensional information (Burrows et al. 2005). To improve the statistics, we combined the data taken in the 2019 May 10–13 observations (OBSIDs=00010627169, 00010627171, 00010627172, and 00010627173), which correspond to the end of the rebrightening.

The *Swift*/UVOT data were reduced with HEASoft version 6.31.1 and the latest *Swift*/UVOT Calibration Database (CALDB) as of 2021 November. We adopted the cleaned sky-coordinate images of the individual filters: UVW1, UVW2, UVM2, U, and V bands, and performed aperture photometry using the UVOT tool `uvot2pha` included in HEASoft. Here, we defined the source and background regions as circles with a 10" radius centered at the source position and in a blank-sky area, respectively.

2.2 *NuSTAR*

The *NuSTAR* data were downloaded from the HEASARC archive² and reduced with `nupipeline` version 0.4.9 in the *NuSTAR* Data Analysis Software (`nustardas`), utilizing the calibration database (CALDB) version 20191219. The source and background extraction regions were defined as circular regions with a radius of 100" centered on the target position and in a nearby source-free region on the same chip as that of the source, respectively. The spectra of the individual focal plane modules (FPMA and FPMB) were produced through `nuproducts` with standard settings for a point source described in the *NuSTAR* quickstart guide³. We combined the spectra from the FPMA and FPMB with `addascaspec`.

2.3 *NICER*

The *NICER* data were downloaded from the HEASARC archive. We performed pipeline processing using `nicer12` included in HEASoft, referring to the *NICER* CALDB version 20190516. The background spectrum was build with the background estimator tool `nibackgen3C50` and the response matrix file and the ancillary response file were created with the `nicerrmf` and `nicerarf`, respectively, all of which are included in HEASoft.

2.4 OISTER

Optical and near-IR multi-band photometric data were obtained by the OISTER collaboration, which is formed with many small-to-medium size telescopes operated

²<https://heasarc.gsfc.nasa.gov/docs/archive.html>

³https://heasarc.gsfc.nasa.gov/docs/nustar/analysis/nustar_quickstart_guide.pdf

Table 1. X-Ray and UV (*Swift*/UVOT) observation log

Observatory/Instrument (Filters)	Date	Exposure (ks)	Observation ID
<i>Swift</i> /XRT	2019 Mar 16	1	10627140
<i>Swift</i> /UVOT (UVM2)	2019 Mar 16	1	10627140
<i>Swift</i> /XRT	2019 Mar 17	2	10627141
<i>Swift</i> /UVOT (U, V, UVM2, UVW1, UVW2)	2019 Mar 17	0.1 each	10627141
<i>Swift</i> /XRT	2019 Mar 24	2	10627148
<i>Swift</i> /UVOT (U, V, UVW1)	2019 Mar 24	0.1 each	10627148
<i>Swift</i> /UVOT (UVM2, UVW2)	2019 Mar 24	0.3 each	10627148
<i>Swift</i> /XRT	2019 Mar 29	0.6	10627150
<i>Swift</i> /XRT	2019 Apr 10	0.7	10627158
<i>NICER</i> /XTI	2019 Apr 30	2.6	2200120329
<i>NuSTAR</i> /FPMA, FPMB	2019 May 1	42 (FPMA), 41(FPMB)	90501320002
<i>Swift</i> /XRT	2019 May 10–13	4	10627169/171/172/173
<i>Swift</i> /UVOT (U, UVM2, UVW1, UVW2)	2019 May 11	0.1 each	10627171

Table 2. Optical and near-IR observation log

Observatory/Instrument (Filters)	Date	Exposure (ks)	Observation ID
OISTER (g)	2019 Mar 16		
LCO, ogg [†] (iVR)	2019 Mar 16	0.2 each	65, 66, 67
OISTER (g)	2019 Mar 17		
LCO, cpt [†] (gr)	2019 Mar 29	0.2 each	171, 173
LCO, cpt (y)	2019 Mar 29	0.3	172
LCO, elp [†] (ri)	2019 Apr 9	0.06 each	183,186
LCO, elp (y)	2019 Apr 9	0.1	185
LCO, cpt (gri)	2019 May 1	0.06 each	214,215,217
OISTER (JHK)	2019 May 1		
OISTER (grizJHK)	2019 May 10		
<i>Seimei</i> /KOOLS-IFU	2019 May 11	0.6 (×15 frames)	
<i>Seimei</i> /KOOLS-IFU	2020 Feb 23	0.3 (×16 frames)	
<i>Seimei</i> /KOOLS-IFU	2020 Mar 18	0.3 (×16 frames)	

[†] The site codes ogg, cpt, and elp indicate Haleakala Observatory, South African Astronomical Observatory, and McDonald Observatory.

by Japanese universities and observatories, including Multicolor Imaging Telescopes for Survey and Monstrous Explosions (MITSuME) at the Akeno Observatory (Kotani et al. 2005; Yatsu et al. 2007; Shimokawabe et al. 2008) and at the Okayama Observatory (Yanagisawa et al. 2010), 55 cm SaCRA telescope at Saitama University (Oasa et al. 2020), and the 2.0 m Nayuta telescope at the Nishi-Harima Astronomical Observatory (Ishiguro et al. 2011; Takahashi et al. 2013).

Using IRAF (Craine 1994; Barden 1995), we conducted standard data reduction procedures including bias and dark subtraction, flat fielding, bad pixel masking, and photometry. The magnitude calibration was performed with nearby reference stars, whose magnitudes were taken from Pan-STARRS1 Surveys (Chambers et al. 2016) for the optical data, and the Two Micron All Sky Survey Point Source Catalog (Cutri et al. 2003) for the near-IR data. Their typical errors were estimated to be $\sim 10\%$ of the resultant flux density.

2.5 LCO

We used archival LCO data of MAXI J1820 in the first rebrightening period. From the science data archive⁴, we downloaded the data processed through the BANZAI pipeline⁵, which performs the standard data reduction of imaging data and aperture photometry using the SExtractor algorithm (Bertin & Arnouts 1996). The data files contain flux values measured using circular apertures with several different fixed radii and those using an adaptively scaled elliptical aperture whose size is determined with the “Kron” radius (Kron 1980). To account for possible ellipticity of the point spread function (PSF) and dependency of PSF size and shape on the source flux and position on the image, we adopted the values from the adaptive elliptical aperture photometry and performed magnitude calibration using nearby stars, referring to the Pan-STARRS1 Surveys (Chambers et al. 2016) for the g, r, i,

⁴ <https://archive.lco.global/>

⁵ <https://lco.global/documentation/data/BANZAIpipeline/>

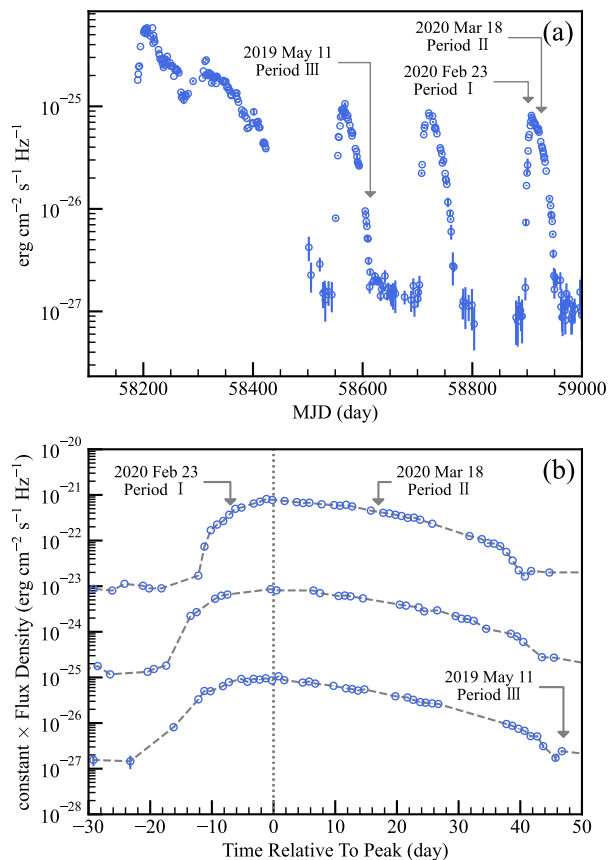


Fig. 1. (a) Optical (g' -band) light curve of MAXI J1820 from the OISTER collaboration (Higuchi et al. in preparation). MJD 58200 corresponds to 2018 March 23. (b) The g' -band light curves in the three rebrightening phases, in which the values on the horizontal axis are adjusted with the flux peaks (MJD 58567, 58721, and 58909 for the first, second, and third rebrightenings, respectively). The flux densities in the second and third rebrightenings are multiplied by 10^2 and 10^4 , respectively, for plotting purposes. The *Seimei* observations are indicated in each panel.

and y bands and the second-generation Guide Star Catalog GSC 2.3 (Lasker et al. 2008) for the V and R bands.

2.6 *Seimei*

We performed optical spectroscopy using the 3.8-m *Seimei* telescope of Kyoto University at the Okayama Observatory (Craine 2010) once in the first rebrightening in 2019 (Yoshitake et al. 2022) and also at two nights in the 2020 rebrightening. In all these observations, we used the Kyoto Okayama Optical Low-dispersion Spectrograph with an integral field unit (KOOLS-IFU; (Yoshida 2005; Matsubayashi et al. 2019)), with the VPH-blue grism, whose wavelength coverage is 4000–8900 Å and the wavelength resolution is $R = \lambda/\Delta\lambda \sim 500$.

The data reduction was conducted with IRAF and the

pipeline tools specifically developed for the KOOLS-IFU⁶ downloaded 2023 July, which performs standard reduction processes including overscan and bias subtraction, flat fielding, wavelength calibration, spectral extraction, sky subtraction, and flux calibration. The Hg, Ne and Xe lamp data were used for the wavelength calibration. In the sky subtraction, we estimated the brightness of the sky from the same object frames using the data of fibers placed on a blank-sky area. The spectra obtained at the same night are averaged into one spectrum.

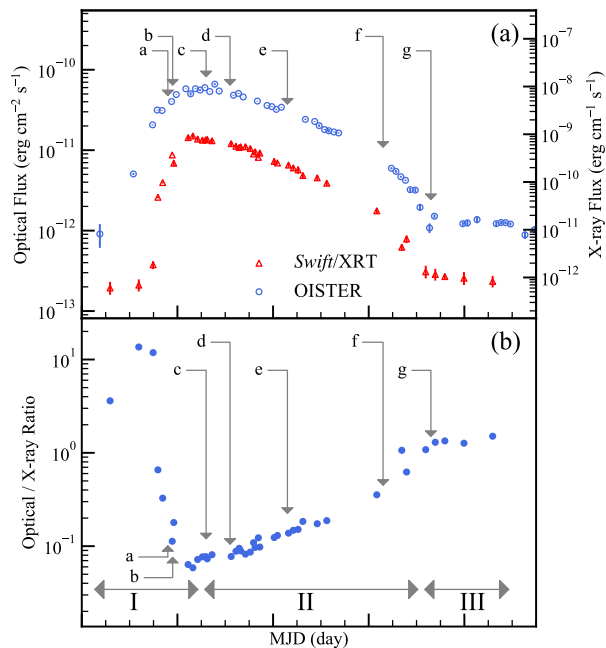


Fig. 2. (a) The g' -band light curve (blue circles) from the OISTER collaboration (Higuchi et al. in preparation) and X-ray light curve from the *Swift*/XRT (red triangles) in the first rebrightening. The X-ray fluxes (in 0.4–10 keV) were estimated from the count rates assuming a power-law shaped spectrum with a photon index of 1.6. The optical fluxes were obtained by multiplying the flux densities in Fig 1 by the g' -band frequency (6.2×10^{14} Hz). (b) The optical versus flux ratio obtained from the data in the panel (a). The horizontal arrows indicate the periods defined based on the behavior of the fluxes and the ratio (Periods I–III; see text). The alphabets a–g with broken arrows show the epochs at which the multi-wavelength SEDs in Figure 4 are obtained.

3 Analysis and Results

3.1 Long-term Light Curves

In Figure 1 we show long-term optical g' -band light curve for about 2 years after the discovery. After the main outburst in 2018, the source showed three rebrightenings. The X-ray data and the UV, optical, and near-IR photometric data were taken in the first (2019) rebrightening, while the

⁶ <http://www.kusastro.kyoto-u.ac.jp/~iwamuro/KOOLS/index.html>

Seimei observations were carried out in the same period and the third (2020) rebrightening. Note that the three rebrightening events have similar light curve profiles, as shown in Figure 1(b).

Figure 2 shows the enlarged view of the first rebrightening period, where X-ray light curve from the Swift/XRT is added. As seen in the top panel, the amplitude of the optical flux rise is larger than that of the X-ray flux. The bottom panel plots the evolution of the optical to X-ray flux ratio, which decreased rapidly during the rising phase, and then increased at a slower rate in the decaying phase. After a discontinuous jump, the flux ratio finally became almost constant in the last period of the rebrightening (where the optical flux declined somewhat more rapidly than before) and then back to the level before the rebrightening. We define these three periods with different behaviors in the optical versus X-ray ratio as Period I (before MJD 58565), Period II (MJD 58565–58611), and Period III (after MJD 58611), which correspond approximately to the flux rise, decay, and dim periods, respectively.

3.2 Multi-wavelength SED

Using the X-ray spectra and the UV to near-IR photometric data listed in Table 1 and 2, we created multi-wavelength SEDs on 2019 March 16, 17, 24, 29, Apr 9–10, Apr 30–May 1, and May 10–13 (hereafter we call Epoch a–g, in time order). We adopted the epochs that have X-ray data and at least 3 near-IR/optical/UV band data. Epochs (a) and (b) are included in Period I and the remaining epochs are in Period II, except for Epoch (g), which is in Period III. Analysis of the SEDs was conducted with XSPEC version 12.13.0c, and the UV to near-IR data were converted to the XSPEC format using `ftflx2xsp`.

We first focused on the Epoch (c) data, which were obtained around the flux peak and have the best statistics and broadband coverage. As a first step, we considered the X-ray spectrum alone and fitted it with a simple absorbed power-law model. We adopted `TBabs` for the absorption model, assuming the abundance table given by Wilms et al. (2000). As shown in Figure 3(a), this model was found to give an acceptable fit with a reduced chi-squared of 316 for 255 degrees of freedom. The best-fit photon index was $\Gamma = 1.53 \pm 0.03$, which is consistent with that in a typical LHS. We obtained the best-fit absorption column density N_{H} of $(1.3 \pm 0.1) \times 10^{21} \text{ cm}^{-2}$, which is consistent with previously reported values using the Swift/XRT or NICER spectra at brighter states in the main outburst (e.g., Uttley et al. 2018; Shidatsu et al. 2018; Rodi et al. 2021) and rebrightenings (Shaw et al. 2021a). This value is also consistent with the Galactic column density estimated from

the H I map ($N_{\text{H}} = 1.3 \times 10^{21} \text{ cm}^{-2}$, HI4PI Collaboration et al. 2016). In the following analysis, we fixed N_{H} of the `TBabs` component at this value.

We then analyzed the multi-wavelength SED in Epoch (c). Here, we adopted the irradiated disk model `diskir` (Gierliński et al. 2008, 2009), which is often used for multi-wavelength SEDs in the LHS, and actually employed in previous works of MAXI J1820 (e.g., Shidatsu et al. 2018; Özbey Arabacı et al. 2022). The `diskir` model considers the multi-color disk emission and its Comptonization, which illuminate the inner and outer disk regions. The irradiation strengths of the inner and outer regions are parameterized with f_{in} and f_{out} , which is the fraction of bolometric flux which is thermalized in the inner and outer disk, respectively. Here, we ignored the illumination of the inner disk (i.e., $f_{\text{in}} = 0$). The f_{out} was allowed to vary within 1×10^{-3} and 1×10^{-2} , a typical range of value in the LHS (e.g., Gierliński et al. 2009). The electron temperature of the Comptonization component was fixed at 65 keV, following Özbey Arabacı et al. (2022). We left the following parameters as free parameters: the inner disk temperature T_{in} , the photon index Γ of the Comptonization component, the ratio of luminosity $L_{\text{c}}/L_{\text{d}}$ in the Comptonization component to the unilluminated disk component, the ratio of outer and inner disk radius $\log(R_{\text{out}}/R_{\text{in}})$, and normalization. We set the upper limit of R_{out} to be the tidal truncation radius, $2.5 \times 10^6 \text{ km}^7$, which we assumed to be 0.8 times the Roche lobe size of the black hole (e.g., Boffin 2001). The Roche lobe size can be estimated to be $3.2 \times 10^6 \text{ km}$ from the Kepler’s third law and Equation (4) in Paczyński (1971) assuming an orbital period of 0.68 day, a black hole mass of $7M_{\odot}$ and a companion mass of $0.5M_{\odot}$ (Torres et al. 2020).

In addition, the `bbodyrad` model is also incorporated to the model to account for the blackbody emission from the companion star. Here we assumed a blackbody temperature of $\sim 4700 \text{ K}$ and a radius of $0.65 R_{\odot}$ considering the results from optical spectroscopy in a low luminosity state (Torres et al. 2019b). We also added the `TBabs` and `redden` components to the full model to account for the interstellar absorption in the X-ray band and extinction in the near-IR to UV band, respectively. We assumed $E(B - V)$ for `redden` to be 0.16 (Baglio et al. 2018). Combining the above components, we obtained `TBabs*redden*(diskir+bodyrad)` model. Fitting the data with this model yielded a chi-squared value of 394 with 257 degree of freedom.

⁷ To realize this, we modified the `diskir` code so that the normalization is parameterized by R_{out} instead of R_{in} (i.e.; $\text{norm.} = (R_{\text{out}}(\text{km}))^2 / D_{10} \cos i$, where D_{10} represents the distance in units of 10 kpc.

We also tested an alternative possibility: the UV-to-near-IR flux is dominated by the jet emission, instead of the irradiated outer disk emission as assumed in the `diskir` model. We adopted the broken power-law model (`bknpower` in XSPEC) as a phenomenological model of the jet synchrotron spectrum, in which the power-law components above and below the break correspond to the optically thin and thick synchrotron emissions, respectively. Here, the photon index above the break was fixed at $\Gamma = 1.7$, which is a typical value of the optically thin synchrotron spectrum (e.g., Russell et al. 2010), while that below the break was allowed to vary. To account for the cooling break, we combined the multiplicative cutoff power-law model `highcut`. We assumed both the optically thin-to-thick spectral break and the cooling break of the synchrotron emission were located between UV and X-ray bands where no data are available, and fixed the break energy of `bknpower` and the cutoff energy at 1×10^{-2} keV and 3×10^{-2} keV, respectively. We combined an additional power-law component to take into account the X-ray emission from hot inner accretion disk, and considered the interstellar absorption/extinction and blackbody emission from the companion star in the same manner as in the `diskir` model. This model, `TBabs*redden*(highcut*bknpower+powerlaw+bbbodyrad)`, produced a much better fit than that of the `diskir` model, with a chi-squared value of 329 for 256 degrees of freedom. Figure 3(c) shows the data and the best-fit model and Table 3 lists the best-fit parameters.

In the above analysis, we found that the observed SED was better described by the jet model than the irradiated disk model. In reality, however, the irradiated outer disk emission should be present as suggested by the optical emission lines detected in the rebrightening phases (see Section 3.3). We therefore tested also the combined jet plus irradiated disk model: `TBabs*redden*(highcut*bknpower+diskir+bbbodyrad)`. We found that the quality of fit obtained from this model ($\chi^2 = 329$ with degrees of freedom of 256) was not improved from the jet model. Table 3 gives the best-fit parameters of this model. As shown in Figure 3(c), the contribution of the `diskir` component to the optical and UV fluxes is a factor of $\gtrsim 5$ smaller than that of the jet synchrotron component.

Next, we performed SED fitting for the rest of the data in Period I and II, using the jet model (`TBabs*redden*(highcut*bknpower+powerlaw+bbbodyrad)`). We note that the `diskir` plus jet model was also tested but the fit was not improved significantly and resulted in a negligible contribution of the `diskir` component to the optical and UV bands. We fixed N_{H} of `TBabs` at

$1.3 \times 10^{21} \text{ cm}^{-2}$ as we did for the SED in Epoch (c). As shown in Figure 4, the model successfully reproduced all the Period-I and Period-II data. The best-fit parameters are listed in Table 4.

The Epoch (g) were analyzed in Yoshitake et al. (2022), where we found that the SED profile is best interpreted by the ADAF model. Following Yoshitake et al. (2022) we used the cutoff power-law model (`cutoffpl`) as an approximated model of the synchro-cyclotron emission from the ADAF, which mainly contributes to the optical band, and a power-law model to represent the thermal bremsstrahlung and/or Comptonization of the synchro-cyclotron emission. Adding a jet component and the blackbody emission from the companion star in the same way as Period-I and II data, we adopted the `TBabs*redden(highcut*bknpower+cutoffpl+powerlaw+bbbodyrad)` model. Figure 4(g) presents the SED data and the best-fit model and Table 4 lists the best-fit parameters, which are consistent with those in Yoshitake et al. (2022).

3.3 Optical Spectrum

In Figure 5 we show the *Seimei* spectra obtained in the three epochs, in which the $\text{H}\alpha$ ($\lambda = 6563 \text{ \AA}$) and $\text{H}\beta$ ($\lambda = 4861 \text{ \AA}$) lines are clearly detected. A weak He I ($\lambda = 5876 \text{ \AA}$) emission line is also seen on 2020 Feb 23 and March 18, and other He I and He II emission lines are identified especially on 2020 Mar 18. These He lines are weaker than the Balmer lines, and the He I line at $\lambda = 5876 \text{ \AA}$ is partly overlapped with the atmospheric Na D absorption features ($\lambda = 5890 \text{ \AA}$ and $\lambda = 5896 \text{ \AA}$), making it difficult to separate the individual contributions and determine the He I line profile accurately. We therefore focused only on the two Balmer lines and investigated their spectral profiles.

Figure 6 shows the $\text{H}\alpha$ and $\text{H}\beta$ spectra obtained with the *Seimei* telescope. On 2019 May 11, which is 47 days after the g' -band flux peak and corresponds to Period III, only emission lines are visible, whereas broad absorption structures are seen in $\text{H}\alpha$ and $\text{H}\beta$ spectra on 2020 Feb 23. On 2020 March 18 the absorption structures still exist but less significant than those in Feb 23. Considering the similarity of the optical g' -band light curve in 2019 and 2020 rebrightening events, we investigated which of three periods (Period I, II, and III) the two observations in 2020 correspond to. On the basis of the number of days from the g' -band flux peak, we found that the observations on 2020 Feb 23 and March 18 are -7 days and $+17$ days from the peak and can be included in Period I and II, respectively (see Figure 1b).

To characterize the line profiles, we performed model

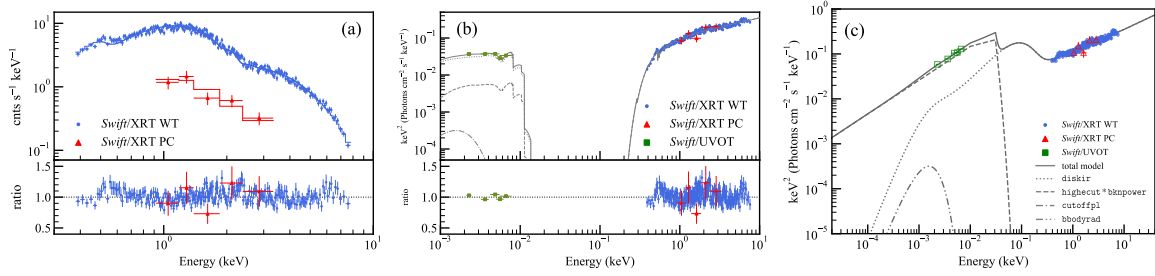


Fig. 3. (Left) X-ray spectrum in Epoch (c) and its best-fit absorbed power-law model. (Middle) multi-wavelength SEDs and best-fit `highcut*bknpower+diskir+bbodyrad` model in Epoch (c). The bottom panel shows the data versus model ratio. (Right) same as the middle panel, but corrected for interstellar extinction. Solid, dotted, dashed, and dot dashed lines show the total model and the `diskir`, `highcut*bknpower`, and `bbodyrad` components, respectively. The blue circles, red triangles, green squares present the Swift/XRT data in the WT mode, those in the PC mode, and the Swift/UVOT data, respectively.

Table 3. Best-fit parameters of the SED fitting in Epoch (c), with the jet and `diskir` model

Date		N_{H}	$\text{Flux}_{\text{opt}}^{\text{jet}}$ *	Γ_{jet}	$L_{\text{opt}}^{\text{jet}}$ *
		10^{21} cm^{-2}	$10^{-12} \text{ erg cm}^{-2} \text{ s}^{-1}$		erg s^{-1}
Epoch	MJD	T_{in}	f_{out}	Γ_{diskir}	L_{X}^*
		keV			erg s^{-1}
$\chi^2/\text{d.o.f}$		R_{out}	$R_{\text{out}}/R_{\text{in}}$	R_{in}	$L_{\text{c}}/L_{\text{d}}$
		r_{g}^{\dagger}		r_{g}	
	2019 Mar 24	1.3 (fixed)	$2.1^{+0.1}_{-0.2} \times 10^2$	1.3 ± 0.1	1.6×10^{35}
(c)	58566	$(3.1 \pm 0.1) \times 10^{-2}$	$1.0^{+2.5}_{-0(\text{pegged})} \times 10^{-3}$	1.54 ± 0.02	6.0×10^{35}
	328/256	$2.4^{+0(\text{pegged})}_{-1.1} \times 10^5$	$1.0^{+1.0}_{-0(\text{pegged})} \times 10^3$	$2.4^{+0(\text{pegged})}_{-1.7} \times 10^2$	$9.9^{+0.1(\text{pegged})}_{-5.6}$

`TBabs*redden*(highcut*bknpower+diskir+bbodyrad)`, with N_{H} of `TBabs` and $E(B-V)$ of `redden` fixed at $1.3 \times 10^{21} \text{ cm}^{-2}$ and 0.16, respectively. For the `bbodyrad` component, $T_{\text{bb}} = 4700 \text{ K}$ and $R_{\text{bb}} = 0.65 R_{\odot}$, and $D = 3 \text{ kpc}$ were assumed. For the `diskir` component, the electron temperature of the Comptonization component was fixed at 65 keV, the fraction of bolometric flux thermalized in the inner disk f_{in} at 1.2×10^{-3} , and the radius of the Compton illuminated disk in terms of the inner disk radius at 1.005. We assume $D = 3 \text{ kpc}$, $i = 70^\circ$, and $M = 7 M_{\odot}$ in order to estimate R_{in} , R_{out} , and the luminosity of the `diskir` component.

* Unabsorbed luminosity and flux of each component in 0.5–5 keV and 0.5–5 eV.

\dagger Gravitational radius $r_{\text{g}} \equiv GM/c^2$ (where G is the gravitational constant and c is the light velocity). r_{g} is 10.5 km assuming $M = 7 M_{\odot}$.

fitting of the $\text{H}\alpha$ and $\text{H}\beta$ spectra on XSPEC. We adopted a wavelength range of 6400–6700 Å for the $\text{H}\alpha$ data and 4750–4950 Å for the $\text{H}\beta$ data and converted them with the `ftool ftflx2xsp` to the XSPEC format. The response matrix files were generated with the `ftool ftgenrsp`, which assumes a Gaussian response function for each wavelength bin. To account for the spectral resolution of the *Seimei*/KOOLS-IFU, we adopted a full width at half maximum (FWHM) of 9.41 Å, 8.29 Å, and 11.14 Å in the $\text{H}\alpha$ spectra and 19.24 Å, 12.61 Å, and 7.35 Å in the $\text{H}\beta$ spectra for the Gaussian response functions on 2019 May 11, 2020 Feb 23, and 2020 Mar 18, respectively. These values were estimated from the profile of a Ne line around the $\text{H}\alpha$ line and a Hg line around $\text{H}\beta$ line in the arc lamp frame.

We fitted the continuum with a single power-law model and adopted a Gaussian model with a negative normalization for the broad absorption component. Some of the emission lines, especially the $\text{H}\alpha$ line on 2019 May 11 and

the $\text{H}\beta$ lines, show a clear flat-topped or double-peaked profile, which is often seen in the emission lines from the accretion disk. The peak-to-peak separation of the $\text{H}\beta$ line on 2020 March 18, which most clearly shows a double-peaked profile, was estimated to be $17 \pm 3 \text{ Å}$. For these emission line components, we employed the `diskline` model (Fabian et al. 1989). The `diskline` model calculates the emission line profile originating from the Keplerian accretion disk illuminated by the X-rays from the inner disk region. We note that the `diskline` model calculate the line profile in almost the same way as the Horne & Marsh (1986) model, often used in the optical line modelling; it computes the Doppler shifts of the individual part of the accretion disk and integrates their contributions over the entire line emitting region of the disk, assuming that the emissivity depends on the radius r as r^α . The `diskline` model considers the relativistic effects in the vicinity of the black hole, but they are negligible at large radii. Following Yoshitake

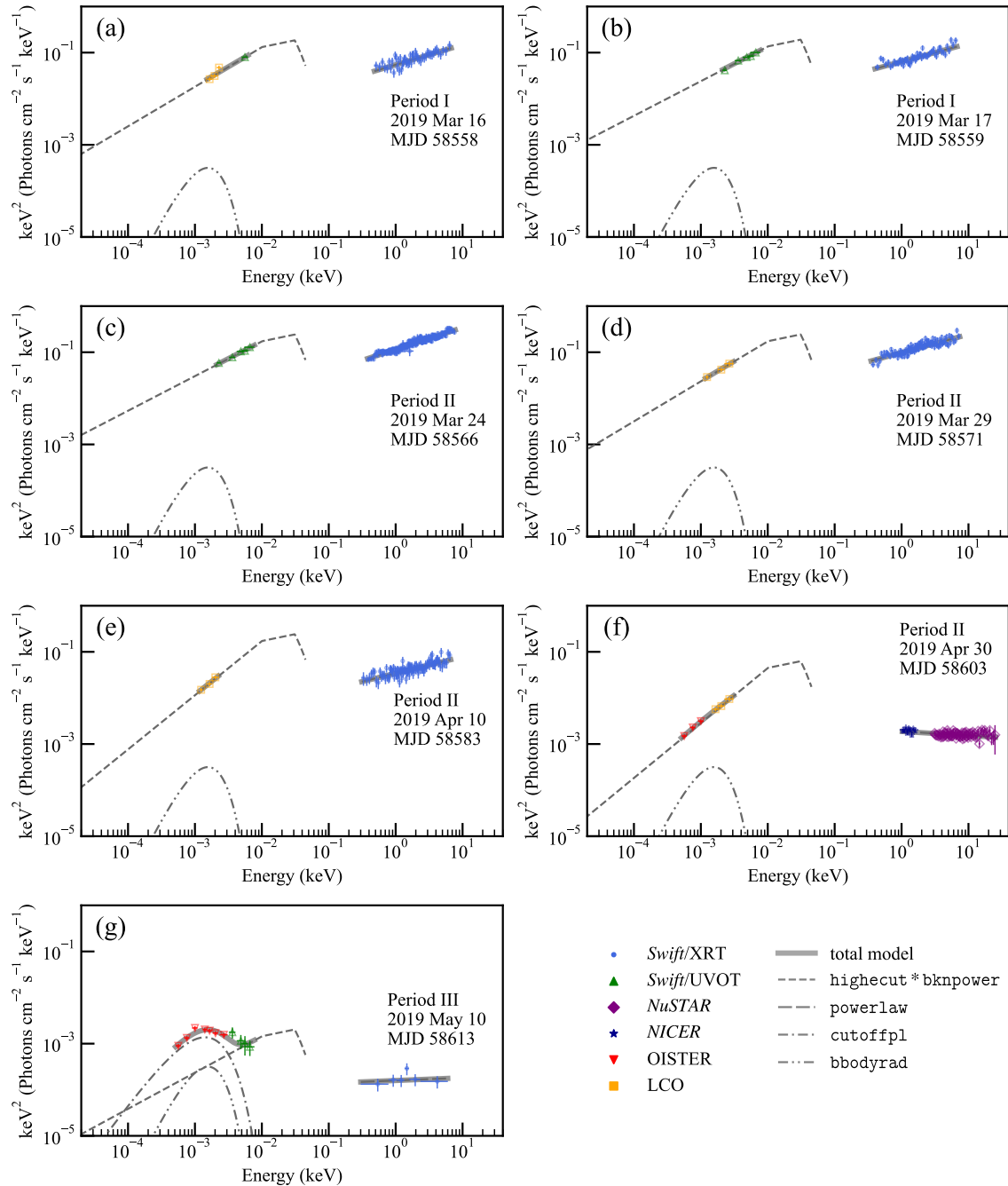


Fig. 4. The multi-wavelength SEDs and best-fit models corrected for interstellar extinction. The *Swift*/XRT, *Swift*/UVOT, *NuSTAR*, *NICER*, OISTER, and LCO data are shown in blue circles, green triangles, purple diamonds, dark blue stars, red inverse triangles, and orange squares, respectively. The adopted models are $\text{highcut} * \text{bknpower} + \text{powerlaw} + \text{bbodyrad}$ for Period I and II, and $\text{highcut} * \text{bknpower} + \text{cutoffpl} + \text{powerlaw} + \text{bbodyrad}$ for Period III. Solid, dashed, dot-double-dashed, dot dashed, and double-dot-dashed lines indicate the total model, and the $\text{highcut} * \text{bknpower}$, powerlaw, cutoffpl, and bbodyrad components, respectively.

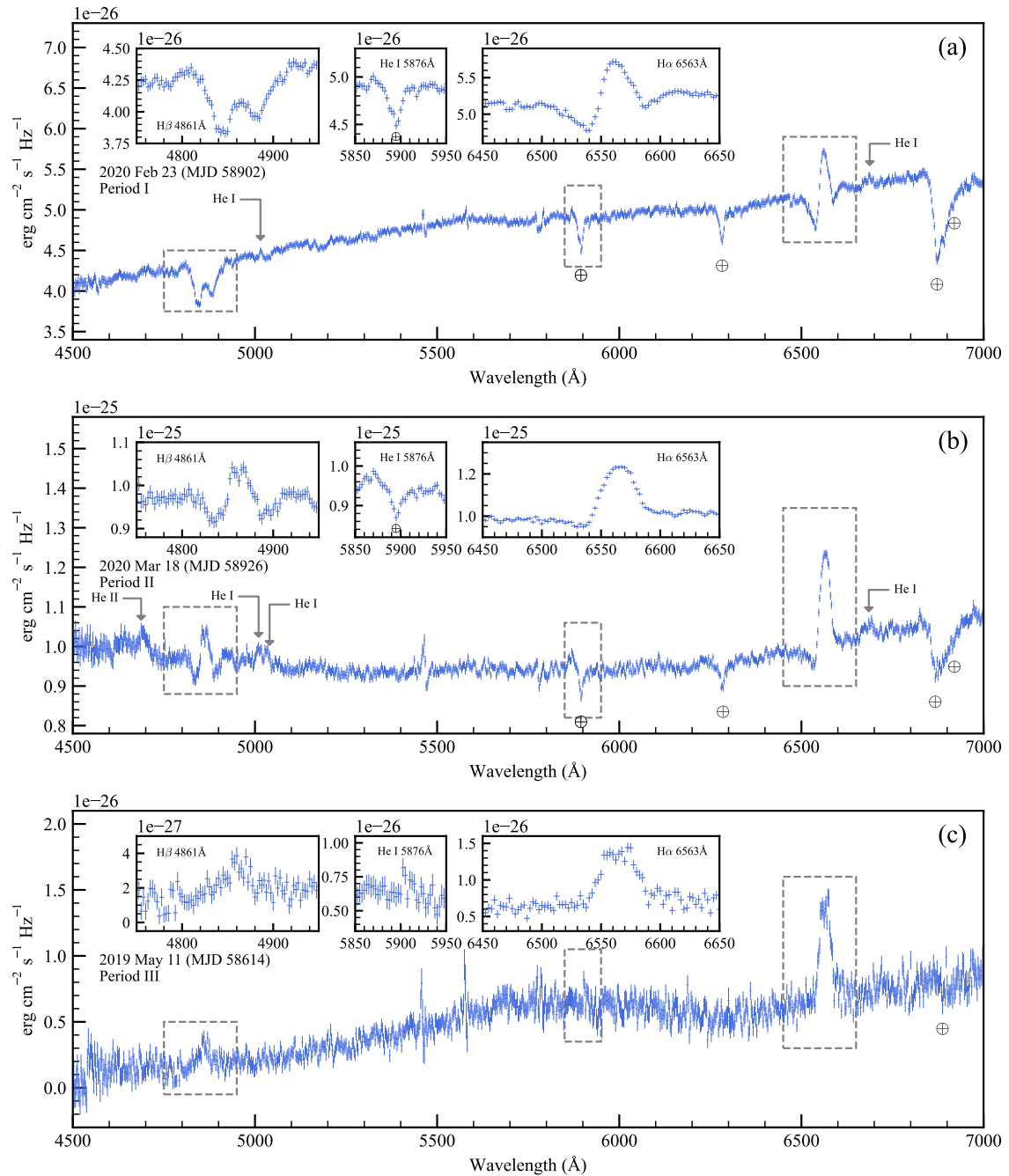


Fig. 5. *Seimei* spectra obtained in the three epochs. The panels (a), (b), and (c) correspond to Period I, II, and III, respectively. The inset panels show enlarged views around $\text{H}\alpha$ ($\lambda = 6563 \text{\AA}$), $\text{H}\beta$ ($\lambda = 4861 \text{\AA}$), and He I ($\lambda = 5876 \text{\AA}$) lines. Other identified lines are also shown with grey arrows.

Table 4. Best-fit parameters of the SED fitting with the jet model

Date		N_{H}	Γ_{jet}	$\text{Flux}_{\text{opt}}^{\text{jet}*}$	$L_{\text{opt}}^{\text{jet}*}$
		10^{21} cm^{-2}		$10^{-12} \text{ erg cm}^{-2} \text{ s}^{-1}$	erg s^{-1}
Epoch	MJD		Γ_{brems}	$\text{norm}_{\text{brems}}$	L_{X}^*
		$\chi^2/\text{d.o.f}$	$E_{\text{peak,ADAF}}$	$\text{norm}_{\text{ADAF}}$	erg s^{-1}
		Period I (rise)			
(a)	2019 Mar 16	1.3 (fixed)	1.1 ± 0.1	$(1.3 \pm 0.1) \times 10^2$	1.3×10^{35}
	58558		1.6 ± 0.1	$2.0^{+0.6}_{-0.5} \times 10^{15}$	2.8×10^{35}
	42/49		-	-	
(b)	2019 Mar 17	1.3 (fixed)	1.2 ± 0.1	$(1.6 \pm 0.1) \times 10^2$	1.5×10^{35}
	58559		1.6 ± 0.1	$2.6^{+0.5}_{-0.4} \times 10^{15}$	3.1×10^{35}
	68/62		-	-	
		Period II (decay)			
(c)	2019 Mar 24	1.3 (fixed)	1.2 ± 0.1	$(2.0 \pm 0.1) \times 10^2$	1.9×10^{35}
	58566		1.53 ± 0.02	$(3.9 \pm 0.2) \times 10^{15}$	6.0×10^{35}
	327/259		-	-	
(d)	2019 Mar 29	1.3 (fixed)	1.1 ± 0.4	$(1.7 \pm 0.2) \times 10^2$	1.6×10^{35}
	58571		1.60 ± 0.03	$(3.9 \pm 0.4) \times 10^{15}$	4.8×10^{35}
	152/128		-	-	
(e)	2019 Apr 10	1.3 (fixed)	$0.8^{+0.5}_{-0.6}$	$1.1^{+0.4}_{-0.3} \times 10^2$	1.0×10^{35}
	58583		1.6 ± 0.1	$(1.5 \pm 0.3) \times 10^{15}$	1.6×10^{35}
	79/102		-	-	
(f)	2019 Apr 30	1.3 (fixed)	0.81 ± 0.13	$(2.7 \pm 0.3) \times 10^1$	2.6×10^{34}
	58603		2.1 ± 0.03	$(2.3 \pm 0.3) \times 10^4$	7.2×10^{33}
	94/87		-	-	
		Period III (dim)			
(g)	2019 May 10–13	1.3 (fixed)	$1.2^{+0.6}_{-2.0}$	$1.5^{+1.4}_{-1.3}$	5.2×10^{33}
	58613		1.9 ± 0.3	$3.5^{+2.9}_{-1.7} \times 10^4$	6.5×10^{32}
	13/11		$7.1^{+1.5}_{-0.8} \times 10^{-4}$	$4.8^{+1.5}_{-2.4} \times 10^4$	

TBabs*redden*(highcut*bknpower+powerlaw+bbbodyrad) (Period I and II) and **TBabs*redden*(highcut*bknpower+cutoffpl+bbbodyrad)** (Period III). The save values as those in Table 3 were adopted for the fixed parameters (see text).

* Unabsorbed luminosity and flux of each component in 0.5–5 keV and 0.5–5 eV.

et al. (2022), we adopted $i = 70^\circ$ and $\alpha = -3$. The outer disk radius R_{out} of the emitting region is assumed to be $2.4 \times 10^5 r_g$, which is estimated in Section 3.2. We allowed the inner disk radius R_{in} to vary. The $\text{H}\alpha$ lines on 2020 Feb 23 and Mar 18 were fitted with a Gaussian model.

Figure 6 shows the results of the data and their best-fit models. Table 5 gives the line widths (half width at zero intensity; HWZI), the equivalent widths, and the inner radius R_{in} of the line-emitting/absorbing regions estimated in the fit. For Gaussian components we adopted their 5σ values as the HWZIs and calculated R_{in} assuming the Kepler motion as

$$R_{\text{in}} \approx 0.87 \left(\frac{\sin i}{\sin 70^\circ} \right)^2 \left(\frac{\text{HWZI}}{\lambda_{\text{rest}}} \right)^{-2} r_g, \quad (1)$$

where λ_{rest} is the rest frame wavelength of the line. For the **diskline** component, we adopted the best-fit R_{in} value

and estimated the HWZI value using Equation 1.

As shown in Figure 6, the line centers of the $\text{H}\alpha$ absorption line in Epoch II and the $\text{H}\beta$ absorption lines in Epoch I and II are consistent with the rest frame wavelengths. The exception is the $\text{H}\alpha$ line on 2020 Feb. 23 (Period I), which shows a blueshift. However, the shift is only within $\sim 10 \text{ \AA}$ (corresponding to $\lesssim 500 \text{ km s}^{-1}$), which is somewhat smaller than the typical value ($\gtrsim 1000 \text{ km s}^{-1}$) of disk winds detected in the optical band (e.g., Muñoz-Darias et al. 2016), and the absorption line is deep and wide compared with usual P Cygni profiles. As seen in Figure 5, the He I line show no significant blueshifted absorption component, either.

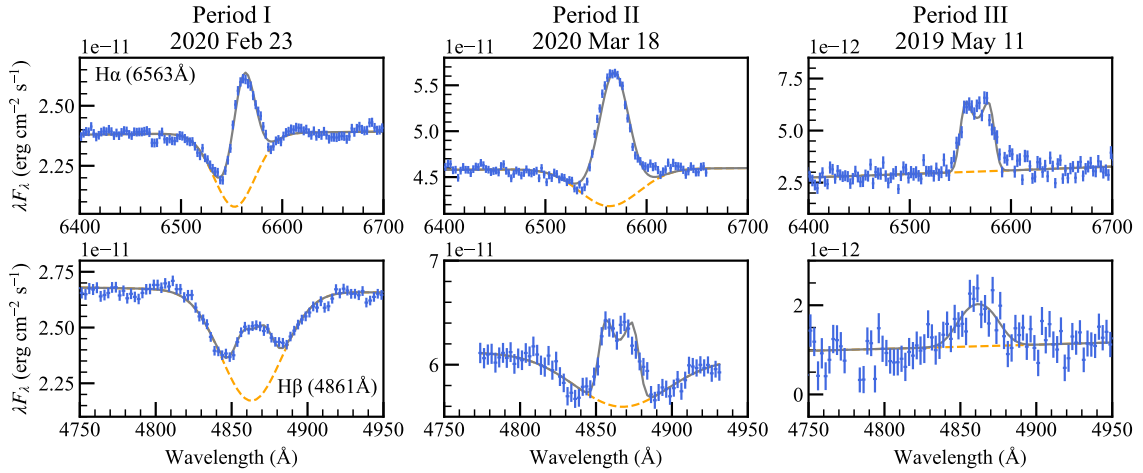


Fig. 6. *Seimei*/KOOLS-IFU spectra around the $H\alpha$ and $H\beta$ lines and their best-fit models. Gray solid and orange dashed lines present the total model and the sum of the continuum and absorption line components, respectively. Note that the data and the model include broadening due to the response of the grism.

Table 5. The best-fit line widths and equivalent widths of $H\alpha$ and $H\beta$ lines, and inner radii of the their emitting/absorbing regions

Period	Date Time Relative To Peak (day)	Line		HWZI (\AA)	Equivalent Width (\AA)	R_{in} (r_g)
I	2020 Feb 23	$H\alpha$	Emis.	53 ± 1	6.1 ± 0.2	$(1.3 \pm 0.1) \times 10^4$
			Abs.	99^{+5}_{-3}	6.5 ± 0.2	$3.8^{+0.2}_{-0.4} \times 10^3$
	-7	$H\beta$	Emis.	11^{+1}_{-2}	3.2 ± 0.7	$1.7^{+0.8}_{-0.3} \times 10^5 \dagger$
			Abs.	96^{+7}_{-6}	9.2 ± 0.7	$(2.3 \pm 0.3) \times 10^3$
II	2020 Mar 18	$H\alpha$	Emis.	66 ± 1	12.3 ± 0.2	$8.7^{+0.3}_{-0.4} \times 10^3$
			Abs.	$(1.1 \pm 0.1) \times 10^2$	6.5 ± 0.4	$2.9^{+1}_{-2} \times 10^3$
	+17	$H\beta$	Emis.	14^{+2}_{-1}	3.5 ± 0.3	$1.1^{+0.1}_{-0.2} \times 10^5 \dagger$
			Abs.	$(1.5 \pm 0.1) \times 10^2$	6.2 ± 0.8	$8.8^{+1}_{-1} \times 10^2$
III	2019 May 11	$H\alpha$	Emis.	18 ± 1	36 ± 2	$1.2^{+0.2}_{-0.1} \times 10^5 \dagger$
			Abs.	-	-	-
	+47	$H\beta$	Emis.	13^{+7}_{-5}	26 ± 5	$1.2^{+1.8(\text{pegged})}_{-0.7} \times 10^5$
			Abs.	-	-	-

\dagger The inner radii R_{in} with the dagger marks are estimated with `diskline`, while the others are calculated from 5σ width of the Gaussian model assuming a Keplerian rotation (see text).

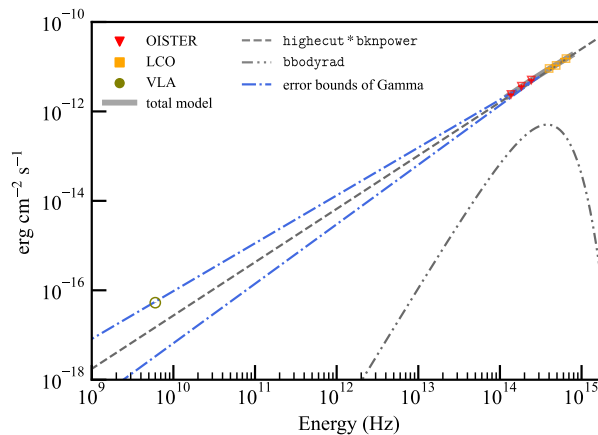


Fig. 7. Optical-UV SED and the best-fit model in Epoch (f) (same as Figure 4(f) but the X-ray band is ignored), with radio data obtained with VLA on the same day. The black solid line shows the best-fit broken power-law component (below the break) for the jet, which is extrapolated to the radio band. The blue dash dotted lines are obtained by changing the photon index to its 90% upper and lower limits.

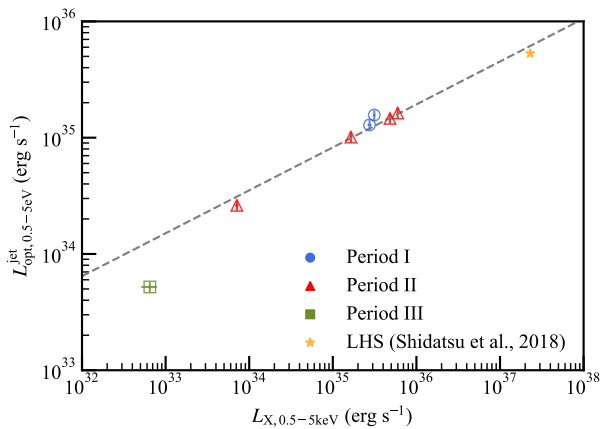


Fig. 8. Correlation of the unabsorbed X-ray luminosity and optical jet luminosity of MAXI J1820. The blue circles, red triangles, green squares, and yellow star show the data taken in Period I, II, and III, and in the LHS of the main outburst (Shidatsu et al. 2018), respectively.

4 Discussion

4.1 SED

4.1.1 Periods I and II

We find that all X-ray spectra in Periods I and II are well represented with a power law model modified with interstellar absorption, confirming previous works on a part of the data analyzed here (Shaw et al. 2021b; Yoshitake et al. 2022; Özbey Arabacı et al. 2022). The power-law dominant X-ray spectra indicate that MAXI J1820 was always in the LHS and no transition to the HSS took place, which is also evident from the hardness ratio estimated in Figure 1 of Stiele & Kong (2020). The LHS is consistent with the low Eddington ratios throughout the rebrightening phase, $\log \lambda_{\text{Edd}} < -3$; usually transition from the LHS to the HSS in the initial outburst phase of a BHXB takes place typically at $\log \lambda_{\text{Edd}} > -2$ (e.g., Maccarone 2003; Vahdat Motlagh et al. 2019). The photon index was about 1.6 in Epochs (a)–(e) when the source was relatively bright ($\log L_X/L_{\text{Edd}} \sim -3$), whereas it became larger (2.1) at a fainter state ($\log L_X/L_{\text{Edd}} \sim -6$). This trend agrees with past studies reporting negative correlations between the photon index and Eddington ratio at $-6.5 < \log L_X/L_{\text{Edd}} < -3$ in BHXBs (Yang et al. 2015).

We have shown that the near-IR/optical/UV SEDs in Periods I and II are reproduced by the sum of the blackbody component from the companion star and a dominant power-law component with a partial contribution from the irradiated disk. The photon indices of the power-law components in Epochs (a)–(d), $\Gamma = 1.1\text{--}1.4$ (corresponding to the energy indices $\alpha = 0.1\text{--}0.4^8$), are consistent with that of the averaged SED during the initial outburst reported by

Tetarenko et al. (2021). In Epochs (e) and (f), the photon indices are somewhat smaller, $\sim 0.7\text{--}0.8$. The reason is unclear; synchro-cyclotron emission from the hot flow, similar to that predicted by an ADAF model (see Section 4.1.2), might partially contribute to the optical flux at high frequencies in these epochs.

We interpret that the origin of the optical power-law component is synchrotron radiation from jets. In fact, the energy indices we have obtained, $-0.4 \lesssim \alpha \lesssim -0.3$, are consistent with that expected from an optically thick jet ($\alpha \sim 0$ for a Blandford-Königl-type conical jet; Blandford & Königl 1979). A viscous disk without irradiation (MCD model) predicts smaller values, $\alpha \approx -0.3$ at the flat part between the blackbody peak frequencies emitted from the outermost and innermost radii, and $\alpha = -2$ below it (Rayleigh-Jeans regime). An irradiated disk predicts $\alpha \sim -1.2$ (e.g., Hynes 2005), although it depends on disk geometry such as the outer disk radius (R_{out} in diskir) and irradiation efficiency (f_{out}) (see e.g., Shidatsu et al. 2011a). On the basis of the SED fitting results for Epoch (c), we conclude that the contribution from the irradiated disk is likely not a dominant source of the optical/UV flux.

To reinforce the interpretation that this component is a jet origin, we compare the optical-UV SED in Epoch (f) with the radio flux density at 6 GHz observed with the Very Large Array (VLA) on the same day (Shaw et al. 2021b). Figure 7 plots the radio to UV SED, where we extrapolate the power-law component determined by the optical-UV SED to lower frequencies. As noticed, the radio flux is consistent with the extrapolation within the uncertainty in the spectral slope. This supports our interpretation that this component is synchrotron radiation from the jets. Within the wavelength coverage of our SED in the optical-UV region, we detect neither a power-law spectral break (corresponding to the optically thin to thick transition frequency) nor a high energy cutoff in the the synchrotron emission (corresponding to the maximum energy of non-thermal electrons in the jets) and have only an lower limit for it ($> 8 \times 10^{-3}$ keV).

Figure 8 plots the X-ray luminosity (L_X) versus the optical luminosity of the jet component ($L_{\text{opt}}^{\text{jet}}$). We also add the data point observed in a brighter LHS in the initial outburst, taken from Figure 9 in Shidatsu et al. (2018). As noticed, a clear positive correlation is found, which can be represented by $L_{\text{opt}}^{\text{jet}} \propto L_X^{0.4}$. The correlation is similar to what is found between the X-ray and radio luminosities in the LHS of BHXBs (e.g., Corbel et al. 2013), and is consistent with the jet interpretation (Russell et al. 2006). We note that similar correlations are expected also from X-ray irradiated disks (e.g., van Paradijs & McClintock 1994), although this model is not supported by the SED

⁸ $F_\nu \propto \nu^{-\alpha}$ where F_ν is the energy flux at frequency ν

fitting (Section 3.2).

In this paragraph, we focus on the results of Epoch (c) obtained with the `bknpower*highcut + diskir` model, where the parameters of `diskir` are well constrained thanks to the good quality X-ray spectrum covering the 0.4–10 keV range. The best-fit parameters are consistent with those reported by Özbey Arabacı et al. (2022) except for the innermost disk temperature and the disk radius parameter. In our best-fit SED, the multi-color disk (MCD) component from the standard disk is dominant at the Extreme UV band, with the innermost temperature (T_{in}) of 3.1×10^{-2} keV in Epoch (c). The X-ray spectrum, which shows no evidence for a soft excess, gives a tight upper limit for T_{in} (< 0.4 keV). We must make caveats, however, that the best-fit SED we obtain might be model dependent since the peak wavelength of the MCD component is not covered by the observed data. Bearing that in mind, we discuss implications from the best-fit MCD parameters below. The innermost radius is estimated to be 2.6×10^3 km from the normalization of the MCD component, suggesting that the standard disk is truncated at $2.5 \times 10^2 r_g$. Such a truncated disk is considered to be a general feature of accretion flow in the LHS of BHXBs (e.g., Tomsick et al. (2009); Shidatsu et al. (2011b); Yamada et al. (2013)). It is noteworthy that the truncation radius is about 10 times larger than that reported by Shidatsu et al. (2018) ($\sim 24 r_g$) in the LHS when the X-ray luminosity was about 30 times brighter than our Epoch (c). This suggests that the innermost radius of a truncated disk increases with decreasing mass accretion rate in the LHS.

4.1.2 Period III

As noticed from Figure 4, the SED in Epoch (g) (Period III) shows different features from those in Periods I and II. A sharp peak is observed in the optical band, and the flux ratio between the optical and X-ray bands is much larger than those in the previous periods. The analysis of the SED in Epoch (g) (Period III) was performed in Yoshitake et al. (2022), but for completeness we present shortly the main points here. Synchro-cyclotron radiation by hot electrons is dominant in the optical band, whereas the X-ray emission is produced by thermal Bremsstrahlung and Comptonization of the synchro-cyclotron photons by the same electrons (e.g., Narayan & Yi 1995, Manmoto et al. 1997). The relation of the optical jet luminosity and the X-ray luminosity in Epoch (g) is also plotted in Figure 8. As noticed, it generally follows the relation obtained in the LHS at brighter flux levels. A slight offset from it is not surprising because the inner disk structure and X-ray emitting mechanism are not the same between the LHS and the ADAF state.

4.2 Balmer Line Profiles

The profiles of Balmer emission and absorption lines in the optical spectra (Figure 6) give important clues to understand the disk structure. In general, absorption lines are formed from the surface of an accretion disk with normal temperature gradient in vertical directions to the disk plane (i.e., decreasing temperature with height), whereas emission lines are produced from that with “inverted” temperature structure (Jimenez-Garate et al. 2002; Hiroi et al. 2009). In X-ray binaries, such temperature inversion can be produced by strong irradiation of X-ray/UV emission from the innermost region.

As an alternative possibility, a disk wind, outflowing gas launched from the disk surface, can produce a P-Cygni profile, characterized by blueshifted absorption and broad emission features. Typical velocities of the absorption by disk winds in BHXBs are about a few thousands of km s^{-1} (e.g., Muñoz-Darias et al. 2016). In fact, such features were detected in optical-near infrared spectra of MAXI J1820 in the LHS (Muñoz-Darias et al. 2019) and in the HSS (Sánchez-Sierras & Muñoz-Darias 2020) during the main outburst, although they were very shallow. As mentioned in Section 3.3, we are not able to detect clear P-Cygni profiles in our *Seimei* spectra taken during the rebrightening phases. We do not rule out the presence of high-velocity disk winds, however, as detection of such features would require a very high signal-to-noise ratio spectra. In the following, we assume that the main absorption and line features are not produced by a disk wind.

4.2.1 Periods I and II

The line width constrains the inner radius at which the line is emitted or absorbed, by assuming Keplerian motion in the accretion disk, as summarized in Table 5. Here we focus on the results of $H\beta$, because the emission and absorption profiles are well separated (Figure 6). As mentioned above, although the optical spectral observations with *Seimei* were performed in the first and third rebrightening phases, it is possible to combine the results because of the similarities of the light curves. We find that the inner radius of the $H\beta$ emitting region slightly decreased from $\sim 2 \times 10^5 r_g$ in Period I (7 days before the X-ray peak) to $\sim 1 \times 10^5 r_g$ in Period II (17 days after it). This result can be interpreted that the irradiated part of the accretion disk was extended toward inner radii in Period II. It is consistent with the decrease in the equivalent width (EW) of the absorption line in Period II because the area of the unirradiated part (i.e., with normal temperature gradient) had to shrink accordingly. A double-peaked $H\beta$ emission profile is noticeable in Period II, whose peak-to-peak ve-

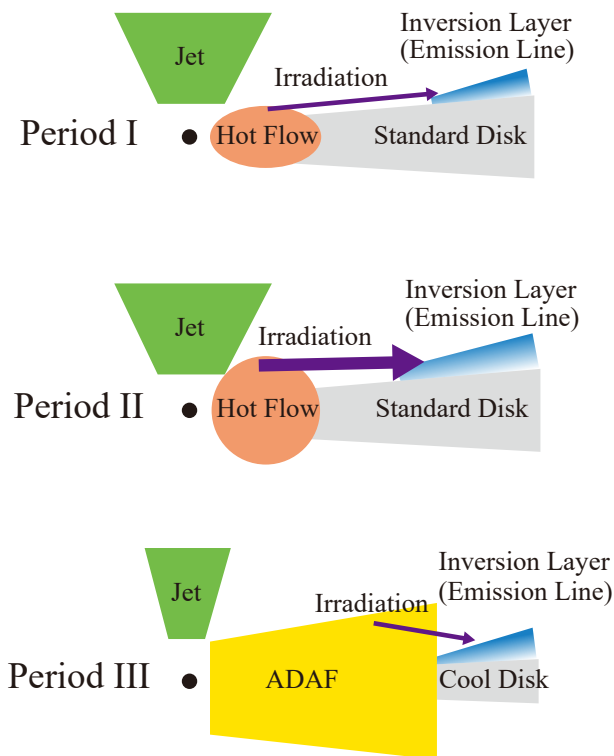


Fig. 9. schematic picture of the accretion disk in the three periods.

locity provides a model-independent estimate of the outer radius of the line-forming region. The half separation of the peaks is estimated to be $8.5 \pm 1.5 \text{ \AA}$, which corresponds to $(3 \pm 1) \times 10^5 r_g$ for $i = 70^\circ$. This is consistent with the Roche lobe size ($3 \times 10^5 r_g$), which is adopted as R_{out} in our `diskline` fitting (Section 3.3).

Broad Balmer absorption plus narrow emission features are often observed in BHXBs during outbursts (e.g., GRO J0422+32, Casares et al. 1995; GRO J1655–40, Soria et al. 2000; XTE J1118+480, Dubus et al. 2001; XTE J1859+226, Zurita et al. 2002; MAXI J1807+132, Jiménez-Ibarra et al. 2019). The absorption lines are thought to arise in the accretion disk at smaller radii (as evidenced by their higher velocities) than the emission lines. In our case, estimated HWZI values of $H\beta$ absorption indicate the innermost radii of $\sim (0.6 - 4) \times 10^3 r_g$ (Table 5). Dubus et al. (2001) suggested that the broad absorption lines were formed by any combination of a low X-ray luminosity, a hard X-ray spectrum, or a low inclination (see their Section 4.1). In our case (MAXI J1820 in the rebrightening phase), the first two conditions are satisfied.

Using our best-fit models (Figure 6), we calculate the equivalent widths (EWs) of $H\alpha$ and $H\beta$ emission lines with respect to the “pseudo” continua (i.e., those not including absorption features) to be $6.1 \pm 0.2 \text{ \AA}$ and $3.2 \pm 0.7 \text{ \AA}$ (Period I) and $12.3 \pm 0.2 \text{ \AA}$ and $3.5 \pm 0.3 \text{ \AA}$ (Period II),

respectively. These values are within the range of those in the LHS during the main outburst reported by Sai et al. (2021), which showed large variability (by a factor of ~ 3 within <10 days). Recalling that the jet component was dominant in the optical band in Periods I and II, the EWs with respect to the “disk” components are estimated to be 2.5–5 times larger than the above values, on the basis of the SED fitting result of Epoch (c) with f_{out} free. According to a Monte-Carlo radiative transfer simulation of an irradiated accretion disk in the HSS of MAXI J1820 by Koljonen et al. (2023), an emission line of $H\alpha$ with a few tens of \AA can be produced in the reprocessed component by disk atmosphere. Considering various uncertainties in the observations (e.g., time variability, modelling of the line profiles) and in theoretical calculations (e.g., differences in the SED and disk structure between the LHS and HSS), we infer that our results do not contradict with the theoretical predictions.

4.2.2 Period III

In Period III, only emission lines are detected in the $H\alpha$ and $H\beta$ regions (see also Yoshitake et al. (2022), who reported a detailed analysis of the $H\alpha$ profile). Its width indicates that the line emitting region is similar to that in Period II ($\sim 10^5 r_g$). Yoshitake et al. (2022) interpret that it is likely to be produced from an optically-thick disk in the “cool” mode. The absence of absorption features suggests that an optically-thick disk in the “hot” mode is not present in this state. This is consistent with our SED model, where no MCD component is included.

4.3 Evolution of Accretion Disk Structure

Interpreting the results on the SED and Balmer line profiles, we illustrate our view on the evolution of accretion disk structure during the rebrightening phase in Figure 9. Note that jets emitting synchrotron radiation in the radio-to-UV band are always present in the system, which are omitted in the figure. In Periods I (rising phase) and II (slowly decaying phase), the overall disk structure is similar to each other. The standard disk is truncated before reaching the ISCO, probably at $\sim 100 r_g$ around the peak flux. Below the truncation radius, it turns into a “hot flow”, which emits X-rays by Comptonizing seed photons from the truncated disk. In Period I, hot corona is less developed compared with Period II probably because the accretion flow in the innermost region does not reach equilibrium yet. This explains the small X-ray to optical luminosity ratios in Period I. Also, X-ray irradiation to the outer disk is limited at large radii in Period I probably because of geometrical effects (e.g., small scale height of the

corona). In Period III (dim phase), the standard disk in the hot mode no longer exists and the whole region at $\lesssim 10^5 r_g$ is replaced by ADAF. The UV and X-ray emission from the ADAF irradiates the outer “cool” disk at $\gtrsim 10^5 r_g$, producing Balmer emission lines. We repeat our caveats, however, that some of the interpretations rely on specific SED modeling under the limited coverage of the multi-wavelength data. Future systematic multi-wavelength observations covering the whole outburst/rebrightening phase are always important to reach robust conclusions on the evolution of the disk structure in BHXBs, and the history of mass accretion rate through the disk. The mechanism of rebrightening phenomena often observed in BHXBs and cataclysmic variables still remains unsolved (e.g. Kato et al. 1998; Hameury et al. 2000; Osaki et al. 2001; Meyer & Meyer-Hofmeister 2015). Those observations will be a key to clarify the rebrightening mechanism.

5 Conclusion

In this work, we have analyzed the broadband (near infrared-optical-UV and X-ray) SED and optical spectra of MAXI J1820 observed in the three rebrightening phases in 2019 and 2020 following the initial outburst in 2018. We find that the rebrightening phase can be classified to 3 periods: (Period I) the “rising” phase before the X-ray flux peak when $F_{\text{opt}}/F_{\text{X}}$ continuously decreased, (Period II) “decaying” phase when $F_{\text{opt}}/F_{\text{X}}$ continuously increased, and (Period III) “dim” phase when $F_{\text{opt}}/F_{\text{X}}$ was roughly constant. The main conclusions are summarized as below.

1. In Periods I and II, MAXI J1820 was always in the LHS, where the X-ray spectrum in the 0.4–10 keV band was approximated by a power law with a photon index of ≈ 1.6 . The near-IR/optical/UV SED was dominated by a power-law with a photon index of $0.7 \sim 1.4$, which smoothly connects to the simultaneous radio flux available in the literature in one epoch. We interpret that that it originates from synchrotron emission from the jets.
2. The $H\alpha$ and $H\beta$ profiles in Periods I and II show broad absorption and narrower emission features. The absorption features are centered close to the rest-frame energy, suggesting that they are not produced by a disk wind. The line widths indicates that the inner radius of an irradiated disk slightly decreased from Period I ($\sim 2 \times 10^5 r_g$) to Period II ($\sim 1 \times 10^5 r_g$), implying evolution of the hot corona geometry.
3. In Period III, we confirm Yoshitake et al. (2022) that the SED can be reproduced by an advection-dominant accretion flow (ADAF) model with jet emission. The Balmer line profiles indicate that an irradiated cool disk was present at $r > \sim 10^5 r_g$.

Acknowledgments

We are very grateful to the anonymous referee for providing many insightful comments to improve the quality of the paper. This research has made use of data and software provided by the High Energy Astrophysics Science Archive Research Center (HEASARC), which is a service of the Astrophysics Science Division at NASA/GSFC. This work made use of public data from the *Swift* data archive. We acknowledge the use of observations from the Las Cumbres Observatory global telescope network. Part of this work was financially supported by Grants-in-Aid for Scientific Research 19K14762 (MS) from the Ministry of Education, Culture, Sports, Science and Technology (MEXT) of Japan, and partially supported by the Optical and Infrared Synergetic Telescopes for Education and Research (OISTER) program funded by the MEXT of Japan.

References

- Baglio, M. C., Russell, D. M., & Lewis, F. 2018, The Astronomer’s Telegram, 11418, 1
- Barden, S. C., ed. 1995, Society of Photo-Optical Instrumentation Engineers (SPIE) Conference Series, Vol. 2476, Fiber Optics in Astronomical Applications, ed. S. C. Barden, 56–67
- Begelman, M. C., McKee, C. F., & Shields, G. A. 1983, ApJ, 271, 70
- Bertin, E., & Arnouts, S. 1996, A&AS, 117, 393
- Blandford, R. D., & Königl, A. 1979, ApJ, 232, 34
- Boffin, H. M. J. 2001, in Astrotomography, Indirect Imaging Methods in Observational Astronomy, ed. H. M. J. Boffin, D. Steeghs, & J. Cuypers, Vol. 573 (Springer), 69
- Burrows, D. N., Hill, J. E., Nousek, J. A., et al. 2005, SSRv, 120, 165
- Casares, J., Martin, A. C., Charles, P. A., et al. 1995, MNRAS, 276, L35
- Chambers, K. C., Magnier, E. A., Metcalfe, N., et al. 2016, arXiv e-prints, arXiv:1612.05560
- Corbel, S., Coriat, M., Brocksopp, C., et al. 2013, MNRAS, 428, 2500
- Craine, D. L. C. E. R., ed. 1994, Society of Photo-Optical Instrumentation Engineers (SPIE) Conference Series, Vol. 2198, Instrumentation in Astronomy VIII, ed. D. L. C. E. R. Craine, 87–97
- . 2010, Society of Photo-Optical Instrumentation Engineers (SPIE) Conference Series, Vol. 7733, Ground-based and Airborne Telescopes III, ed. D. L. C. E. R. Craine
- Cúneo, V. A., Alabarta, K., Zhang, L., et al. 2020, MNRAS, 496, 1001
- Cutri, R. M., Skrutskie, M. F., van Dyk, S., et al. 2003, 2MASS All Sky Catalog of point sources.
- Done, C., Gierliński, M., & Kubota, A. 2007, A&A Rv, 15, 1
- Dubus, G., Kim, R. S. J., Menou, K., Szkody, P., & Bowen, D. V. 2001, ApJ, 553, 307
- Ebisawa, K., Makino, F., Mitsuda, K., et al. 1993, ApJ, 403, 684

- Echiburú-Trujillo, C., Tetarenko, A. J., Haggard, D., et al. 2023, arXiv e-prints, arXiv:2311.11523
- Fabian, A. C., Rees, M. J., Stella, L., & White, N. E. 1989, *MNRAS*, 238, 729
- Gandhi, P., Rao, A., Johnson, M. A. C., Paice, J. A., & Maccarone, T. J. 2019, *MNRAS*, 485, 2642
- Gierliński, M., Done, C., & Page, K. 2008, *MNRAS*, 388, 753
— 2009, *MNRAS*, 392, 1106
- Hameury, J.-M., Lasota, J.-P., & Warner, B. 2000, *A&A*, 353, 244
- HI4PI Collaboration, Ben Bekhti, N., Flöer, L., et al. 2016, *A&A*, 594, A116
- Hiroi, K., Moritani, Y., Nogami, D., et al. 2009, *PASJ*, 61, 697
- Horne, K., & Marsh, T. R. 1986, *MNRAS*, 218, 761
- Hynes, R. I. 2005, *ApJ*, 623, 1026
- Ishiguro, M., Takahashi, J., Zenno, T., Tokimasa, N., & Kuroda, T. 2011, *Annu. Rep. Nishi-Harima Astron. Obs.*, 21, 13
- Jimenez-Garate, M. A., Raymond, J. C., & Liedahl, D. A. 2002, *ApJ*, 581, 1297
- Jiménez-Ibarra, F., Muñoz-Darias, T., Armas Padilla, M., et al. 2019, *MNRAS*, 484, 2078
- Kato, T., Nogami, D., Baba, H., & Matsumoto, K. 1998, in *Astronomical Society of the Pacific Conference Series*, Vol. 137, *Wild Stars in the Old West*, ed. S. Howell, E. Kuulkers, & C. Woodward, 9
- Kawamuro, T., Negoro, H., Yoneyama, T., et al. 2018, *The Astronomer's Telegram*, 11399, 1
- Koljonen, K. I. I., Long, K. S., Matthews, J. H., & Knigge, C. 2023, *MNRAS*, 521, 4190
- Kotani, T., Kawai, N., Yanagisawa, K., et al. 2005, *Nuovo Cimento C Geophysics Space Physics C*, 28, 755
- Kron, R. G. 1980, *ApJS*, 43, 305
- Lasker, B. M., Lattanzi, M. G., McLean, B. J., et al. 2008, *AJ*, 136, 735
- Lasota, J.-P. 2001, *New Astronomy Reviews*, 45, 449
- Maccarone, T. J. 2003, *A&A*, 409, 697
- Makishima, K., Takahashi, H., Yamada, S., et al. 2008, *PASJ*, 60, 585
- Manmoto, T., Mineshige, S., & Kusunose, M. 1997, *ApJ*, 489, 791
- Matsubayashi, K., Ohta, K., Iwamuro, F., et al. 2019, *PASJ*, 71, 102
- Matsuoka, M., Kawasaki, K., Ueno, S., et al. 2009, *Publications of the Astronomical Society of Japan*, 61, 999
- Meyer, F., & Meyer-Hofmeister, E. 2015, *PASJ*, 67, 52
- Mineshige, S., & Wheeler, J. C. 1989, *ApJ*, 343, 241
- Muñoz-Darias, T., Casares, J., Mata Sánchez, D., et al. 2016, *Nature*, 534, 75
— 2017, *MNRAS*, 465, L124
- Muñoz-Darias, T., Jiménez-Ibarra, F., Panizo-Espinar, G., et al. 2019, *ApJL*, 879, L4
- Narayan, R., & Yi, I. 1995, *ApJ*, 452, 710
- Oasa, Y., Ushioda, K., Shibata, Y., et al. 2020, in *Ground-based and Airborne Instrumentation for Astronomy VIII*, Vol. 11447, *International Society for Optics and Photonics*, 114475Z
- Osaki, Y., Meyer, F., & Meyer-Hofmeister, E. 2001, *A&A*, 370, 488
- Özbey Arabacı, M., Kalemci, E., Dinçer, T., et al. 2022, *MNRAS*, 514, 3894
- Paczyński, B. 1971, *ARA&A*, 9, 183
- Rodi, J., Tramacere, A., Onori, F., et al. 2021, *ApJ*, 910, 21
- Russell, D. M., Fender, R. P., Hynes, R. I., et al. 2006, *MNRAS*, 371, 1334
- Russell, D. M., Maitra, D., Dunn, R. J. H., & Markoff, S. 2010, *MNRAS*, 405, 1759
- Sai, H., Wang, X., Wu, J., et al. 2021, *MNRAS*, 504, 4226
- Saikia, P., Russell, D. M., Pirbhoy, S. F., et al. 2023, *ApJ*, 949, 104
- Sánchez-Sierras, J., & Muñoz-Darias, T. 2020, *A&A*, 640, L3
- Shakura, N. I., & Sunyaev, R. A. 1973, *A&A*, 500, 33
- Shaw, A. W., Plotkin, R. M., Miller-Jones, J. C. A., et al. 2021a, *ApJ*, 907, 34
— 2021b, *ApJ*, 907, 34
- Shidatsu, M., Nakahira, S., Murata, K. L., et al. 2019, *ApJ*, 874, 183
- Shidatsu, M., Ueda, Y., Tazaki, F., et al. 2011a, *PASJ*, 63, S785
— 2011b, *PASJ*, 63, S785
- Shidatsu, M., Nakahira, S., Yamada, S., et al. 2018, *ApJ*, 868, 54
- Shimokawabe, T., Kawai, N., Kotani, T., et al. 2008, in *American Institute of Physics Conference Series*, Vol. 1000, *Gamma-ray Bursts 2007*, ed. M. Galassi, D. Palmer, & E. Fenimore, 543–546
- Soria, R., Wu, K., & Hunstead, R. W. 2000, *ApJ*, 539, 445
- Stiele, H., & Kong, A. K. H. 2020, *ApJ*, 889, 142
- Takahashi, J., Zenno, T., & Ishiguro, M. 2013, *Bull. Cent. Astron. Univ. Hyogo*, 1, 17–22
- Tanaka, Y., & Shibasaki, N. 1996, *ARA&A*, 34, 607
- Tetarenko, A. J., Casella, P., Miller-Jones, J. C. A., et al. 2021, *MNRAS*, 504, 3862
- Tetarenko, B. E., Shaw, A. W., & Charles, P. A. 2023, *MNRAS*, 526, 6284
- Tetarenko, B. E., Sivakoff, G. R., Heinke, C. O., & Gladstone, J. C. 2016, *ApJS*, 222, 15
- Tomsick, J. A., Yamaoka, K., Corbel, S., et al. 2009, *ApJL*, 707, L87
- Torres, G., Stefanik, R. P., & Latham, D. W. 2019a, *ApJ*, 885, 9
- Torres, M. A. P., Casares, J., Jiménez-Ibarra, F., et al. 2020, *ApJL*, 893, L37
— 2019b, *ApJL*, 882, L21
- Tucker, M. A., Shappee, B. J., Holoiën, T. W. S., et al. 2018, *ApJL*, 867, L9
- Ueda, Y., Inoue, H., Tanaka, Y., et al. 1998, *ApJ*, 492, 782
- Uttley, P., Gendreau, K., Markwardt, C., et al. 2018, *The Astronomer's Telegram*, 11423, 1
- Vahdat Motlagh, A., Kalemci, E., & Maccarone, T. J. 2019, *MNRAS*, 485, 2744
- van Paradijs, J., & McClintock, J. E. 1994, *A&A*, 290, 133
- Wilms, J., Allen, A., & McCray, R. 2000, *ApJ*, 542, 914
- Yamada, S., Makishima, K., Done, C., et al. 2013, *PASJ*, 65, 80
- Yanagisawa, K., Kuroda, D., Yoshida, M., et al. 2010, in *American Institute of Physics Conference Series*, Vol. 1279,

- Deciphering the Ancient Universe with Gamma-ray Bursts,
ed. N. Kawai & S. Nagataki, 466–468
- Yang, Q.-X., Xie, F.-G., Yuan, F., et al. 2015, *MNRAS*, 447,
1692
- Yatsu, Y., Kawai, N., Shimokawabe, T., et al. 2007, *Physica E
Low-Dimensional Systems and Nanostructures*, 40, 434
- Yoshida, M. 2005, *Journal of Korean Astronomical Society*, 38,
117
- Yoshitake, T., Shidatsu, M., Ueda, Y., et al. 2022, *PASJ*, 74,
805
- Zhang, G. B., Bernardini, F., Russell, D. M., et al. 2019, *ApJ*,
876, 5
- Zurita, C., Sánchez-Fernández, C., Casares, J., et al. 2002,
MNRAS, 334, 999